

THE LOMA PRIETA, CALIFORNIA, EARTHQUAKE OF OCTOBER 17, 1989:
EARTHQUAKE OCCURRENCE

MAIN-SHOCK CHARACTERISTICS

MECHANICAL MODELING OF A FAULT-FOLD SYSTEM, WITH
APPLICATION TO THE EARTHQUAKE

By Ze'ev Reches,
Hebrew University, Jerusalem;
and
Mark D. Zoback,
Stanford University

CONTENTS

	Page
Abstract	A183
Introduction	183
Analysis of a fault-fold system	184
Approach	184
Deformation above a faulted rigid basement	184
Reverse basement fault versus normal basement fault ..	185
The 1989 Loma Prieta earthquake	186
Features of the earthquake	186
Modeling the earthquake as a fault-fold system	187
Mechanical layering	187
Model parameters	188
Results	188
Shear zones	188
Aftershock distribution	190
Conclusion: Layered versus uniform medium	190
Acknowledgments	191
References cited	191
Appendix: Analytical procedure	192
Calculation and presentation procedures	193

ABSTRACT

Some features of the deformation accompanying the 1989 Loma Prieta earthquake resemble that associated with earthquakes along deep-seated reverse faults. These features include ground breakage, surface deformation, aftershock distribution, and a component of reverse slip deduced from geodetic and strong-ground-motion data. To explore these deformational features of the earthquake, we derive an analytical model for the deformation of a layered sequence due to slip along a deep-seated fault. Our model includes horizontal elastic layers, using configurations with as many as nine layers of different shear moduli. We applied this layered model to the Loma Prieta region and found that the better solutions are for five-layer sequences in which the shear moduli of the layers increase downward. The model predicts the distribution of aftershocks in the upper 5 km better than a model with

uniform rheology. The model also accurately predicts the location of the zone of horizontal extension in the Summit Road area and the zone of horizontal compression in the northeastern foothills of the Santa Cruz Mountains.

INTRODUCTION

Since the early 1980's, deep-seated faults concealed by folded structures have been recognized as a significant source for seismic hazard (for example, Stein and King, 1984). This recognition reflects observations of the 1980 El-Asnam, Algiers, the 1983 Coalinga, Calif., and the 1987 Whittier Narrows, Calif., earthquakes. In these and other earthquakes, the deep faults form a fault-fold system in which slip along a fault zone at depth appears as a fold or a flexure within the overlying sedimentary layers.

Fault-fold systems have been modeled by using several different methods. One common approach is kinematic analysis, for which the balanced cross section is the best known representative. This technique was developed to analyze large-scale deformation by assuming that rock volume (area in two-dimensional profiles) is conserved during deformation (Dahlstrom, 1969). Using this approach, the initial configuration and even the deformation path can sometimes be reconstructed from the geometry of the final deformed structure. The kinematic approach, however, has some severe limitations: Rock rheology is omitted, rock layers are merely lines drawn on profiles without mechanical properties, and the mechanical differences between layers are ignored. Therefore, although the kinematic analysis maintains geometric compatibility, it could violate known dynamic principles.

Another approach is the modeling of upper-crustal deformation by dislocations within a linear, elastic half-space. This modeling has been extensively used in the inversion of long-term geodetic data, as well as for seismic and postseismic displacements. Although half-space models can provide impressive fits to geodetic data (Lisowski

and others, 1990), they do not incorporate the layering of crustal rocks and are limited to small deformation. For example, King and others (1988) extended such models by considering a thick, linear elastic layer over a viscous half-space; they modeled the development of crustal flexures by many repeating earthquakes, incorporating seismic slip, viscous-isostatic relaxation, erosion, and sedimentation. One surprising result of their analysis is that the calculated elastic thickness of the crust is only 2 to 4 km.

A different approach assumes that slip along deep-seated faults is accommodated within the overlying rocks by flexing, faulting, and tilting, which form such fault-fold systems as monoclines or asymmetric folds (Reches, 1978). Reches and Johnson (1978) derived a general model for the development of a fault-fold system and analyzed the mechanics of draping, buckling, and kinking within the sedimentary sequence. Because crustal rocks commonly display mechanical layering rather than uniform rheology, we believe that relevant models must incorporate this property.

The 1989 Loma Prieta earthquake resulted in several features that resemble the deformational features of earthquakes associated with deep-seated reverse faults: the types of surface deformation and ground breakage, the aftershock distribution, and the large amount of subsurface reverse slip deduced from inversion of geodetic (Lisowski and others, 1990) and strong-ground-motion data (Beroza, 1991). To explore the deformational style in the Loma Prieta region, we have derived a model for a layered rock sequence above a deep-seated fault. The analysis is for horizontal, incompressible, elastic layers subjected to fault-related displacement along the base of the sequence. Our model attempts to reproduce the location and style of surface deformation and aftershock distribution of the earthquake. We compare the results of this layered model with those from the uniform-rheology model.

ANALYSIS OF A FAULT-FOLD SYSTEM

APPROACH

We derive here an analytical solution for a fault-fold system that includes a sequence of layers overlying a basement (fig. 1). The basement is idealized as an elastic half-space that can deform by slip along planar faults; the layered sequence above the fault is idealized as horizontal layers with nonuniform moduli that are either bonded to each other or free to slip along their contacts. In theory, these layers can deform elastically or viscously; the analysis below is for linear, incompressible, elastic layers under plane-strain conditions. Details of the analytical procedure are presented below in the appendix (see Reches and Johnson, 1978).

The computations provide the displacement, stress, and strain fields within the layered sequence. By using a Fourier series of stepped waveforms, the solutions can handle the combination of continuous, periodic folding processes in the layers and discontinuous fault displacements in the basement.

DEFORMATION ABOVE A FAULTED RIGID BASEMENT

We first present the solutions for a simple fault-fold system that is common in regions of moderate tectonic deformation, such as the Colorado Plateaus, the Rocky Mountains, and the Middle East (Prucha and others, 1965; Reches, 1978; Stearns, 1978; Reches and others, 1981). This simple fault-fold system is a zone of flexed, bent, and tilted layers of sedimentary rocks above basement faults (fig. 2). In these structures, the layers are deformed

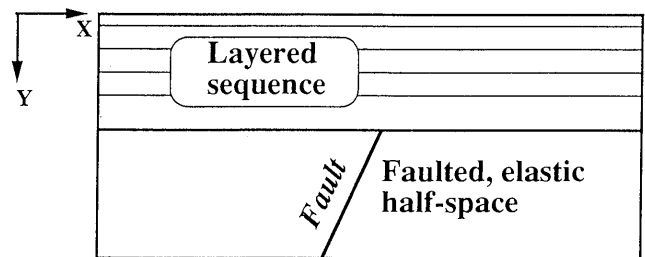


Figure 1.—Idealized geometry of a faulted basement overlain by a layered sequence.

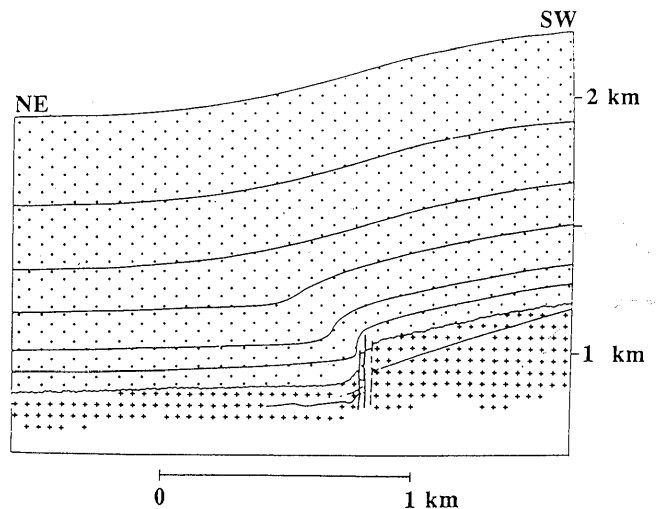


Figure 2.—Simple fault-fold system, showing a profile of the Palisades monocline, Grand Canyon, Ariz. Crosses, Precambrian units; dots, Paleozoic formations. Modified from Reches and Johnson (1978).

and tilted near the fault and almost undeformed and essentially flat away from the fault. The local deformation of the layers reflects the response of the layered sequence in part to the deep-seated faulting (Stearns, 1978) and in part to tectonic stresses within the layers (Reches and Johnson, 1978).

We restrict our analysis to fault-fold systems with small displacements of a few tens to a few hundreds of meters of fault slip. Following King and others (1988), we assume that such systems develop in cycles of seismic events alternating with long periods of interseismic elastic deformation. It is further assumed that in such systems, the interseismic elastic deformation in the basement is relaxed during seismic events, and so the basement may be regarded as rigid. A rigid basement implies that its top on both sides of the fault remains fairly planar and close to horizontal (fig. 2). In contrast, the overlying layers deform permanently by flexing and tilting. In systems with large displacements (>1 km), the basement may not be regarded as rigid because it deflects, owing to isostatic relaxation, erosion, sedimentation, or a combination of these processes (King and others, 1988).

REVERSE BASEMENT FAULT VERSUS NORMAL BASEMENT FAULT

We now present solutions for two idealized fault-fold systems, one with a reverse fault in the basement and the other with a normal fault in the basement (fig. 3). The two systems include six horizontal layers that are bonded to each other along their contacts. Each layer is 200 m thick, and the shear moduli alternate between 6 and 20

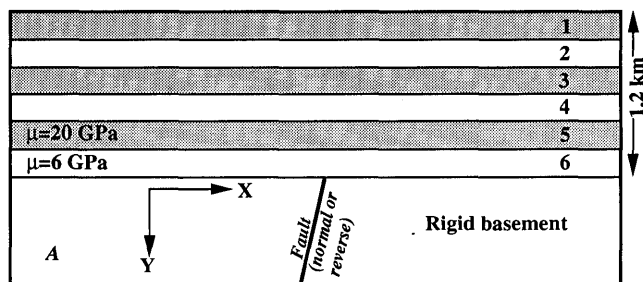


Figure 3.—Analytical solution for deformation of a sequence of six layers above a rigid basement. A, Model configuration: Layers are elastic, incompressible, with bonded contacts, 0.2 km thick; shear modulus alternates between 6 GPa in layers 1 (top), 3, and 5 and 20 GPa in layers 2, 4, and 6 (basal layer). B, Normal fault dipping 60° to right. C, Reverse fault dipping 60° to left. In figures 3B and 3C, fault tip is at 0-m distance (center); 180 wavelengths were used in Fourier series. Continuous curved lines, displacements of contacts between layers (short lines connect initial and final positions); short heavy bars, orientations of σ_1 axes. Gray tones (1–10 scale on right side) indicate intensity of change in normalized shear stress $\Delta\tau_E$ (see appendix, eq. 12).

GPa (fig. 3A). In line with field observations (fig. 2) and the arguments in the preceding subsection, the top of the basement is maintained horizontal and planar during the deformation (which is linear in the two-dimensional approximation used).

The results for a normal fault that dips 60° to the right (fig. 3B) and for a reverse fault that dips 60° to the left (fig. 3C) are shown in figure 3; both systems have 1 m of vertical displacement of the basement. Each solution shows the displacement of the layers, the change in the local shear stress $\Delta\tau_E$ (see eq. 12), and the orientations of the maximum compressive stress induced by slip along the deep-seated fault.

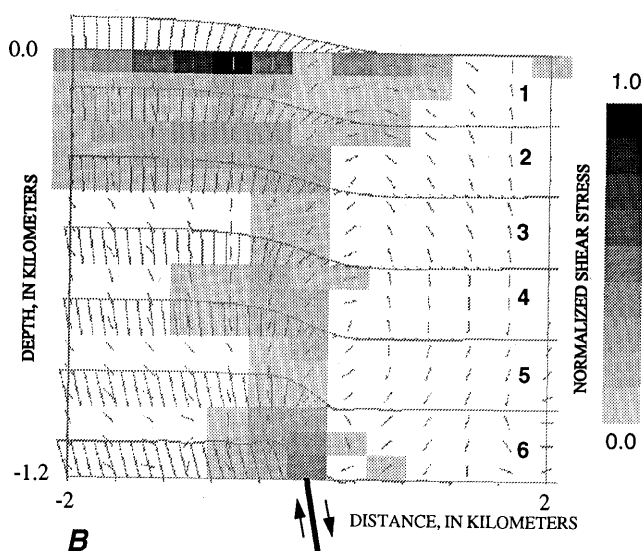


Figure 3.—Continued.

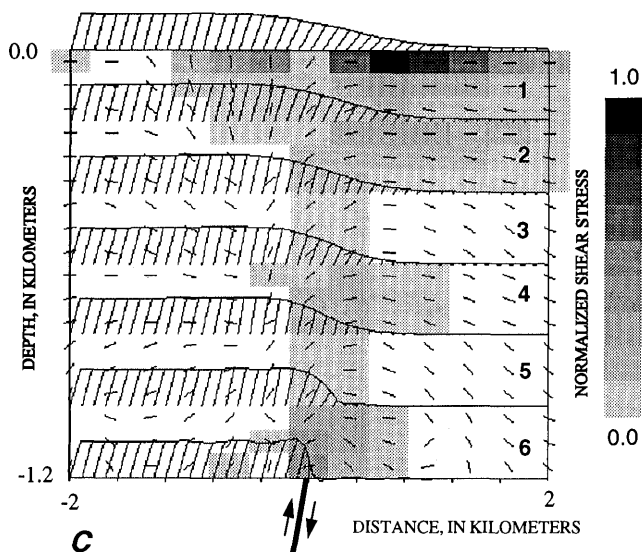


Figure 3.—Continued.

The most conspicuous feature in these solutions is the appearance of a zone of increasing shear stress $\Delta\tau_E$ above the fault (figs. 3B, 3C). The width of this zone varies significantly: It is a few hundred meters wide in the basal layer, about 1 km wide in the central part of the sequence, and a few kilometers wide close to the top (figs. 3B, 3C). Local increases in shear stress and the width of the zone occur within the layers of large shear modulus, layers 2, 4, and 6. This increase reflects the rule of thumb that the stiffer components in nonuniform materials—layered sequences or a medium with inclusions—concentrate the stresses. The stressed zone appears as a continuation of the basement fault: It dips generally to the right for the normal fault (fig. 3B), and to the left for the reverse fault (fig. 3C).

Another significant feature of the solutions shown in figure 3 are the orientations of the principal stresses within the stressed zone. To simplify the variations in the induced stress, we refer to three stress orientations: regions of layer-normal compression, in which the axes of maximum compression are inclined 60° or more to the subhorizontal layering; regions of layer-parallel compression, in which the axes of maximum compression are inclined 30° or less; and regions of layer-parallel shear, in which the axes of maximum compression are inclined 30° – 60° . In the normal-fault system, most regions, particularly those with a relative increase in shear stress, are of the layer-normal compression type (fig. 3B). A region of layer-parallel compression appears to the right of the center, within the synclinal zone of the surface flexure. In the reverse-fault system, the situation is generally inverted, and most regions of shear stress increase with layer-parallel compression (fig. 3C).

These patterns of stress orientations could profoundly affect the structural development. The layer-parallel compression in the reverse-fault system could invoke two deformational modes: propagation of the basement reverse fault, or buckling and flexing of the layered sequence (Reches and Johnson, 1978). Buckling and flexing will prevail if the layers are thin, if considerable differences in elastic moduli exist between the layers, and if the friction along the bedding surfaces is relatively low. Under such conditions, the basement fault will be transformed into a monoclinical flexure in the layered sequence, and a fault-fold system would develop (Reches, 1978). This process of flexure above a fault may explain the absence of surface rupture above some active reverse faults.

The situation is different for the normal-fault system because layered sequences do not buckle under the effect of layer-normal compression. The stresses within the layers above a basement normal fault (fig. 3B) would enhance normal faulting and the propagation of the basement fault into the layered sequence. This process is further enhanced because rocks are significantly stronger under

compression than under extension and the layers above the normal fault are more likely to yield by faulting rather than by folding.

THE 1989 LOMA PRIETA EARTHQUAKE

FEATURES OF THE EARTHQUAKE

The 1989 Loma Prieta earthquake occurred within the San Andreas fault system in the Santa Cruz Mountains, Calif. The hypocenter of the event was about 17 km deep, relatively deep for the San Andreas fault system. The focal-plane solution of the main shock (Oppenheimer, 1990) and the distribution of aftershocks (Dietz and Ellsworth, 1990) indicate that seismic slip occurred along a fault that dips about 70° SW., with mixed reverse and right-lateral slip. This sense was confirmed by inversion of the geodetic measurements, with a best fit of observations to 1.6 ± 0.3 m of right-lateral strike slip and 1.2 ± 0.4 m of vertical reverse displacement (Lisowski and others, 1990). The slip in this earthquake was apparently heterogeneous, as demonstrated by inversion of the strong-ground-motion data (Beroza, 1991). This analysis indicates that the slip can be divided into two separate segments, a northern segment with almost pure reverse slip and a southern segment with almost pure right-lateral slip; for both components, the peak local slip amplitude is 2.8 m (Beroza, 1991). Marshall and others (1991) analyzed the leveling data and considered solutions for two coplanar segments. Their best signal-to-noise ratio was obtained for a two-segment fault, dipping 62° , with a rake of 116° (almost pure reverse slip) in the northern segment and a rake of 163° (almost pure strike slip) in the southern segment.

Surface fractures of apparent tectonic origin were observed in three main zones. The first zone is an area of extensional features along Summit Road, west of Loma Prieta (vertical-lined area, fig. 4; Ponti and Wells, 1991). This zone is about 6 km long and 1 to 1.5 km wide; it is subparallel to the San Andreas fault and 1 to 2 km from its southwest side (the Pacific block). Most of the fractures display mixed displacement: extension normal to the fractures with either left- or right-lateral slip. The maximum measured displacement was 92 cm, with a left-lateral component of 42 cm (Ponti and Wells, 1991). Many of the observed fractures within this zone coincide in position and trend with those mapped by Sarna-Wojcicki and others (1975) and were also active during the 1906 San Francisco earthquake. Several investigators attributed this fracture zone to gravitational sliding, in part relating localization of the fractures to the topographic elevation (Ponti and Wells, 1991).

A second zone is situated along the northeastern foothills of the Santa Cruz Mountains, about 3 to 6 km north-

east of the San Andreas fault (areas C, fig. 4). The dominant features here are fractures with reverse motion and small buckles mostly within manmade structures, such as roads or sidewalks (Plafker and Galloway, 1989).

The third zone includes surface fractures along the main trace of the San Andreas fault, southeast of Loma Prieta. Aydin and others (1992) mapped in detail the fractures here and found primarily fractures with right-lateral motion (max 30 cm) and reverse slip.

MODELING THE EARTHQUAKE AS A FAULT-FOLD SYSTEM

Some of the above-listed observations suggest that the 1989 Loma Prieta earthquake is similar to earthquakes along deep-seated reverse faults. The most relevant observations are the patterns of surface rupture, the occurrence of extensional features in the Pacific block and compressional features in the North American block, and the mixed reverse and right-lateral slip at great depth, with almost pure reverse slip along the northern part of the slipping fault segment. For these reasons, we analyze the deformation associated with slip along the northern part of the Loma Prieta rupture zone as a deep-seated reverse fault. The analyzed models were restricted to a vertical profile trending N. 40° E. (line AB, fig. 4), perpendicular to the

slip surface determined by Dietz and Ellsworth (1990) and Oppenheimer (1990).

MECHANICAL LAYERING

The Loma Prieta region reveals a complex structure composed of major strike-slip faults, reverse faults, and large folds, which are generally subparallel to the San Andreas fault (McLaughlin and others, 1988; Clark and others, 1989). The exposed rocks along the Loma Prieta rupture zone are marine and nonmarine clastic units of Tertiary age that occupy at least the upper 1 km northeast of the San Andreas fault and 2 km or more on the southwest side. Basement rocks are exposed either southwest of the Zayante fault or northeast of the Berrocal fault (McLaughlin and others, 1988; Clark and others, 1989). The sedimentary rocks are intensely deformed by tight and isoclinal folds and faults (mostly reverse). The block between the San Andreas and Sargent faults seems to be more intensely faulted by reverse faults than the block southwest of the San Andreas fault. The layering in the Loma Prieta region has most likely facilitated the regional folding and flexing during the past few million years. However, because the available folding analyses are restricted to inclinations gentler than 10°–15° (Johnson, 1977), it is practically impossible to quantitatively analyze the deformation of the intensely deformed sequence of Loma Prieta in its present structure.

Another layered structure is reflected in seismic profiles of the region. Seismic-velocity models of the Loma Prieta region reveal a low-velocity (3.3–5.8 km/s) wedge between the Zayante and San Andreas faults that extends to depths of more than 8 km (fig. 5B; Eberhart-Phillips and others, 1990). This wedge was interpreted as marine sedimentary rocks of Tertiary age (Eberhart-Phillips and others, 1990). A high-velocity zone (6.4–6.7 km/s) that appears between the San Andreas and Sargent faults was interpreted as mafic intrusive rocks (fig. 5B).

The upper 3 to 5 km of the crust in the study area displays relatively simple, subhorizontal velocity layering (fig. 5A), with a gradual increase in *P*-wave velocity from 3.3 km/s at the surface to about 6 km/s at 5-km depth (fig. 5). This simple velocity layering is apparently unrelated to the complex folded structure of the sedimentary layers. The seismic velocity cannot be correlated with clear lithologic or stratigraphic units, and so the increase in velocity with depth is interpreted as reflecting the compaction and cementation of Tertiary clastic sedimentary rocks.

Following this interpretation of depth-controlled hardening, we consider the profile of seismic velocity (fig. 5) as reflecting mechanical layering in the upper 5 km of the crust. Accordingly, we used a ratio of 0.25 between the

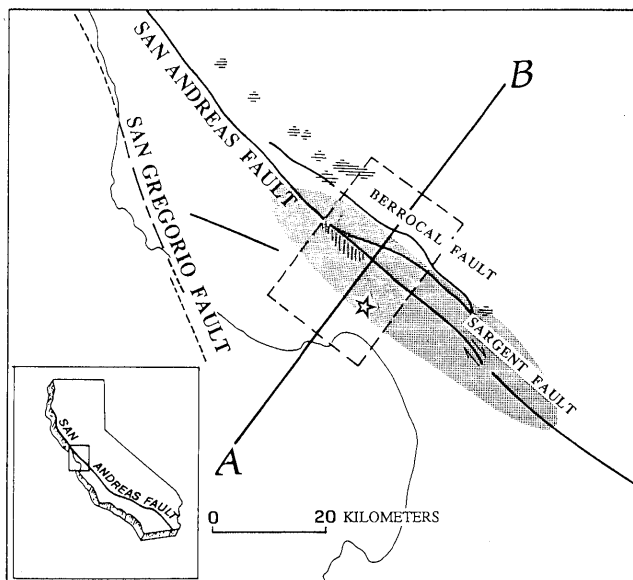


Figure 4.—Area of 1989 Loma Prieta earthquake (modified from Plafker and Galloway, 1989). Star, main-shock epicenter; shaded area, after-shock zone; vertical-lined area, zone of surface rupture with predominantly extensional fractures; horizontal-lined areas, zones of surface rupture with predominantly compressive features; line AB, profile in N. 40° E. direction for present model (see fig. 5); dashed rectangle, area of aftershocks used in present analysis (see fig. 5).

shear modulus of the top layer to the shear modulus of the basal layer, in general agreement with the ≈ 0.5 ratio of P -wave velocities in the top layer to those in the basal layer (fig. 5).

MODEL PARAMETERS

We calculated solutions with layered sequences consisting of one to nine layers and total thicknesses of 3, 5, and 7 km under plane-strain conditions. We examined layers that were either free to slip along their contacts or bonded to each other. The shear moduli of the layers were selected to show (1) a downward increase in modulus, from 4 GPa at the top to 16 GPa at the base; (2) a downward decrease in modulus, from 16 GPa at the top to 4 GPa at the base; or (3) a uniform modulus for the layers free to slip along their contacts. Depth variations of shear moduli were in equal steps according to the number of layers. As the basal displacements are specified (see appendix), the mechanical properties of the basement do not affect the solution. The basal displacement was calculated

with the computer program DIS3D for a reverse slip of 1 m along a 70° -dipping reverse fault (see appendix).

A few groups of solutions were rejected in the early stages of the calculations for the following reasons. First, we correlated zones of increase in shear stress in the solution with zones of high density of aftershocks. Aftershocks of the earthquake were concentrated within a 2- to 3-km-wide zone that extends from 18- to about 1-km depth (Oppenheimer, 1990). The zones of shear-stress increase in an acceptable model should approximately coincide with the zone of high density of aftershocks, and so we rejected models that clearly do not conform to this correlation. In models with free-slip contacts, the upper layers are detached from the displacement at the basement, leading to shear-stress increase within a wide region of the basal layer, with no increase of the shear stresses in the upper layers. Second, models with shear moduli decreasing downward generated shear stress fields that contradicted the aftershock distribution. Furthermore, these models do not conform to the velocity profiles shown in figure 5. Similar contradictions appeared for single-layer solutions with a uniform shear modulus. Therefore, models with free slip between layers, with downward-decreasing moduli, and with uniform shear modulus (fig. 7) were all rejected in early stages of the calculations.

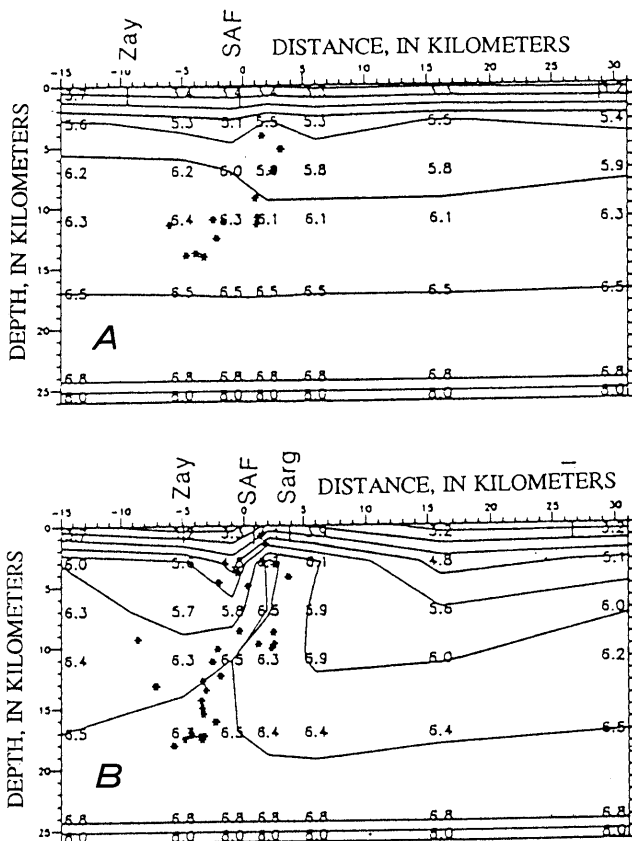


Figure 5.—Seismic velocity structure along southwest-northeast profiles 20 km northwest of main shock epicenter (A) and across main shock (B) (after Eberhart-Phillips and others, 1990).

RESULTS

We found that models with five layers, downward-increasing shear moduli, and bonded contacts fit better the relevant field observations. The results of these models are displayed at different horizontal and vertical scales in figures 6A through 6C, which show the displacement of the layers, the change of the local shear stress $\Delta\tau_E$ (eq. 12), and the orientations of the maximum compressive stress.

SHEAR ZONES

One conspicuous feature of our models is the appearance of two distinct zones of intensive increase in shear stress. The first zone is a subvertical region above the basement fault and slightly to the northeast (fig. 6). This zone reflects the increase in shear stress within the stiffer lower layers, owing to the deformation localized above the fault. The zone is 4 to 5 km wide at the base and narrows to about 1 km wide at 1- to 2-km depth. The orientation of σ_1 , the axis of maximum compression, varies spatially within the zone.

The second zone of shear-stress increase is a horizontal, 10- to 12-km-wide region in the upper layer (fig. 6B); the intense stresses here are restricted to the upper 200 to 300 m (fig. 6C). This second zone largely reflects the low

lithostatic load at shallow depths because $\Delta\tau_E$ is the change in shear stress normalized by the lithostatic stress (see appendix, eq. 12). This zone is separable into two regions: a region of horizontal σ_1 on the northeast side and a region of vertical σ_1 on the southwest side; the positions of maximum shear-stress increase in these two regions are 6 to 7 km apart (fig. 6B). These regions correlate in position with the anticlinal and synclinal bends of the flexure of the top layer. The two regions of increased stresses within the subhorizontal zone (fig. 6B) correlate with the two regions of tectonic surface rupture mentioned above (fig. 4): the Summit Road zone with dominantly extensional fractures and the northeastern foothills of the Santa Cruz Mountains with compressional features. The projection of these two zones onto a N. 40° E. vertical

section near California Highway 17 reveals a distance of 6 to 7 km along the profile, in good agreement with the model calculations (fig. 6). We calculated that the extension normal to the fault across a 4-km-wide zone, centered 2 km west of the San Andreas fault is about 7.5 cm.

Ponti and Wells (1991) noted that many of the major cracks in the Summit Road zone correlate with the local slope direction and are associated with landslides and bedding-plane slippage. They found that the cumulative, fault-normal extension across the fracture zone ranges from 65

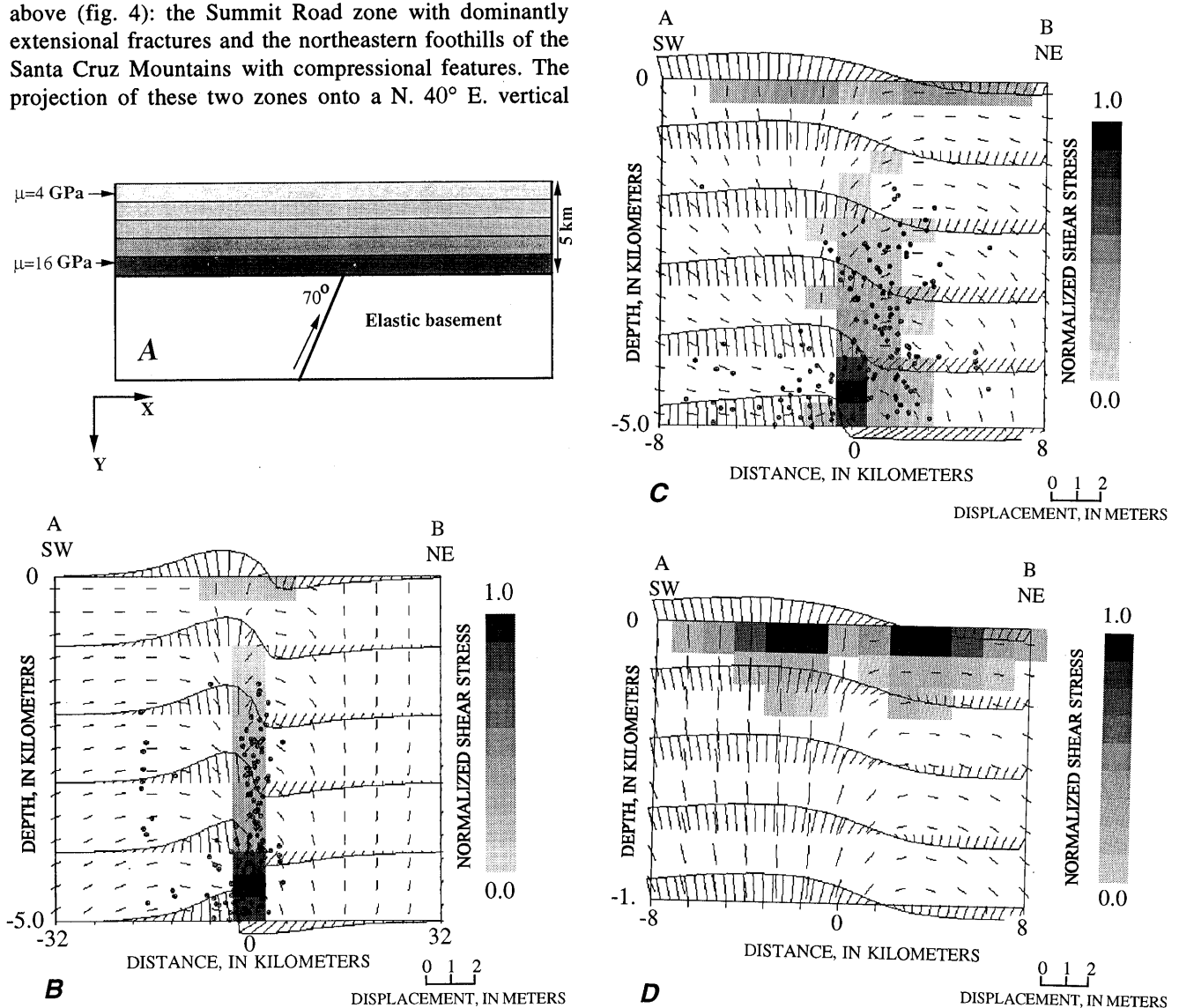


Figure 6.—Analytical solutions at different scales for deformation associated with an earthquake. A, Configuration of preferred model: a sequence of five elastic, incompressible layers, each 1 km thick and bonded to each other. Shear modulus (μ) of top layer is 4 GPa, increasing in equal steps to 16 GPa in basal layer. Basal displacements were calculated for 1 m of reverse slip along a 70°-dipping reverse fault within an elastic basement (see appendix for details). Displacement is transformed in a Fourier series with 160 wavelengths. B, Five-layer sequence. Fault is in center of base. C, Expanded view of figure 6B. D, Upper layer (layer 1). In figures 6B through 6D, fault tip is at 0-m distance (center). Dots, 215 aftershocks for period October 18–31, 1989 (after Dietz and Ellsworth, 1990), with hypocenters projected horizontally to section profile (see text). Continuous curved lines, displacements of contacts between layers (short lines connect initial and final positions); short heavy bars, orientations of σ_1 axes. Gray tones (1–10 scale on right side of fig. 6B) indicate intensity of change in normalized shear stress $\Delta\tau_E$ (see appendix, eq. 12).

to 104 cm (8 to 14 times the extension calculated in the present model). They proposed that the extension is due to ridgetop spreading rather than tectonic deformation.

Our interpretation is that the extension in the Summit Road zone is due to slip during the earthquake which was amplified by local topographic features. Horizontal extension is a common feature associated with the anticlinal bend above a deep-seated normal (fig. 3A) or reverse (fig. 3C) fault. Anticlinal extensional zones were recognized by Sanford (1959), and Reches and Johnson (1978), who applied these zones to analyze the mechanisms of monocline development. The compressional zone in the synclinal bend is the complement to the extensional zone in the anticlinal bend (figs. 3, 6).

We note, however, that the extension-compression pair reflects the *local* stress field associated with slip along the fault; the total stresses are the sum of these local stresses and the *remote* stresses (see appendix). If, for example, the remote stresses are compressional, they would enhance the compressional zone in the synclinal bend and diminish the extensional zone in the anticlinal bend (Reches and Johnson, 1978).

AFTERSHOCK DISTRIBUTION

Another result of our modeling is a prediction of the locations of shallow aftershocks. The locations of aftershocks for the period October 18–31, 1989, are plotted in figure 7. From the list of 1,173 best constrained hypocenters, we selected all 215 events with hypocenters that are no more than 5 km deep and with epicenters inside a frame 20 by 30 km on both sides of our modeling profile (fig. 4). These hypocenters are projected horizontally onto the N. 40° E.–S. 40° W. vertical surface and plotted on the derived solutions.

These aftershocks are well confined to the subvertical zone of shear-stress increase above the fault (figs. 6A, 6B). We examine whether this correlation between the aftershock pattern and the predicted zone of shear-stress increase depends on the layering in the model by calculating a solution for a single layer of uniform rheology (fig. 7); other parameters are the same as in figure 6. It is apparent that the single-layer solution in figure 7 displays a poor correlation between the intensity of the shear-stress increase and the aftershock distribution. The difference between the two solutions reflects the rheologic difference between the models: The lower layers of figure 6 have a high stiffness, and so they tend to be more highly stressed than the less stiff layers above them, whereas in the single-layer solution the shear-stress increase is concentrated at the surface, owing to the effect of the low normal stress (see appendix).

CONCLUSION: LAYERED VERSUS UNIFORM MEDIUM

The deformation associated with earthquakes is commonly calculated for one or more dislocations embedded within a uniform elastic half-space. The analytical solution presented here allows the shear modulus to vary between horizontal layers (fig. 1). By using these solutions, simple, but more realistic (nonuniform), rheologic models can be explored. The models presented here for the Loma Prieta region describe a sequence of layers in which the shear moduli vary by a ratio of 1:4 (fig. 6), in accordance

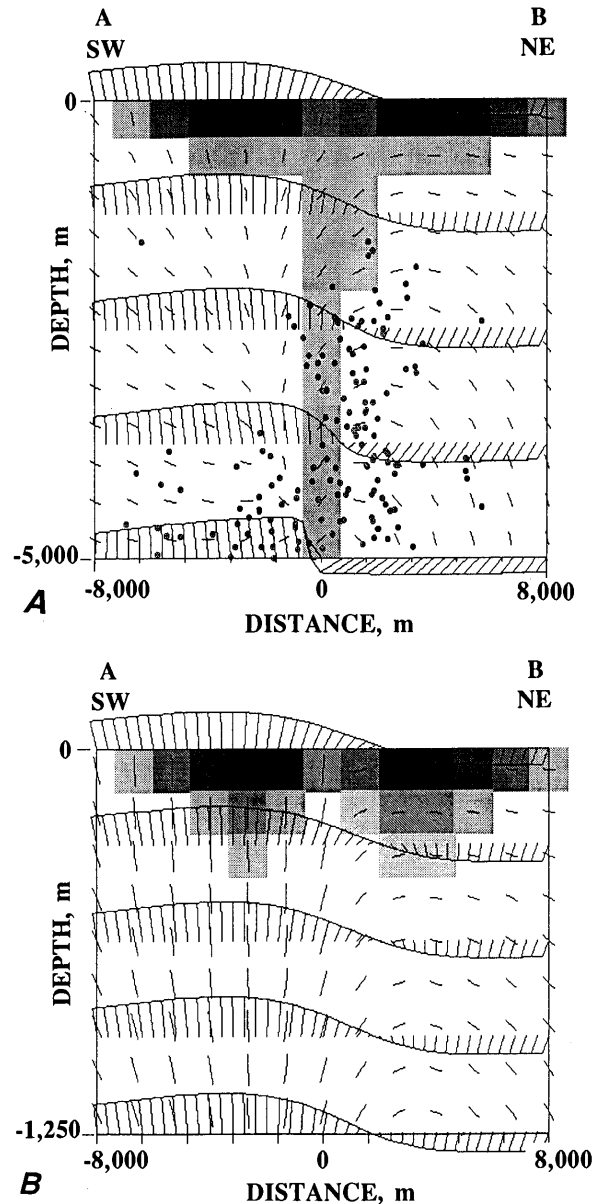


Figure 7.—Analytical solution for deformation of a single elastic layer, 5 km thick. Same basal displacement as in figure 6. A, Profile of entire layer. B, Details of upper 1.25 km. Same symbols as in figure 6.

with the P -wave-velocity ratio ($\approx 1:2$); (fig. 5). The present solutions seem to provide better predictions of the after-shock distribution than the uniform model (compare figs. 6, 7). Both models provide similar explanations for the two zones of surface deformation (extension in the Summit Road zone and compression in the foothill zone; figs. 4, 6B, 7). The present solution indicates that the after-shock zone should be centered between the regions of surface extensional deformation (Summit Road) and surface compressional deformation (foothills) (fig. 6).

We also compared the expected vertical displacement at the ground surface for the layered-medium model and for the uniform-layer model. Figure 8 shows that the vertical displacements in these two models deviate by only 2 to 5 percent from each other. This small difference suggests that leveling data are insensitive to rheologic variations with depth and the existence of layered media.

The present analysis provides a method to study the deformation in a layered medium above a faulted basement. Even the simple geometry of the basic model presented here (fig. 1) may generate a wide variety of stresses and displacements (figs. 3, 6) possibly related to the wide variety of focal-plane mechanisms of the aftershocks. We consider it an important result that the layering used in our preferred model for the 1989 Loma Prieta earthquake is consistent with the mechanical layering revealed by the seismic-velocity structure and that the calculated stresses and displacements agree well with the observed surface deformation and aftershock locations.

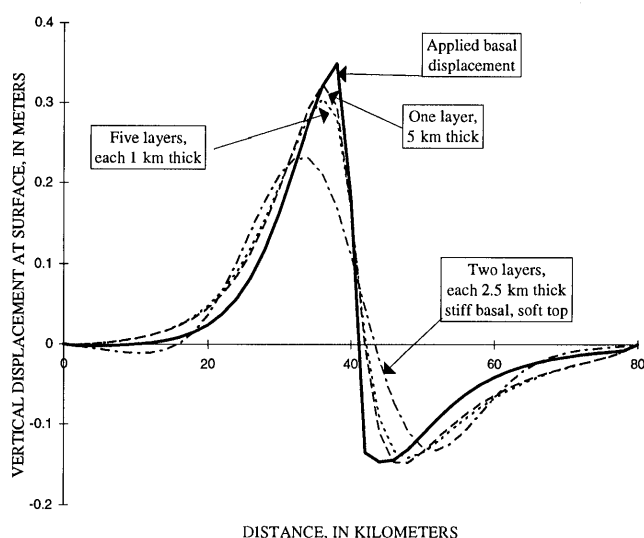


Figure 8.—Vertical displacements associated with a basement reverse fault, dipping 70° to left with 1 m of reverse slip (same conditions as in figs. 6, 7). Total thickness, 5 km; basal layer is 100 times stiffer than upper layer (dotted curve).

ACKNOWLEDGMENTS

This research was supported in part by U.S. Geological Survey grant 14080001-G-1853 to Stanford University. We thank Lynn Dietz of the U.S. Geological Survey for providing the aftershocks listing. Discussions with Paul Segall, Ross Stein, Bill Ellsworth, Dave Oppenheimer, Dan Ponti, Mike Lisowski, and Jim Dieterich are greatly appreciated. The reviews and comments by Ross Stein, Bob Simpson, Joe Andrews, and Paul Spudich contributed significantly to the manuscript.

REFERENCES CITED

- Aydin, A., Johnson, A.M., and Fleming, R.W., 1992, Right-lateral/reverse surface rupturing along the San Andreas and Sargent fault zones during the October 17, 1989, Loma Prieta, California, earthquake: *Geology*, v. 20, p. 1063-1067.
- Beroza, G.C., 1991, Near-source modeling of the Loma Prieta earthquake; evidence for heterogeneous slip and implications for earthquake hazard: *Seismological Society of America Bulletin*, v. 81, no. 5, p. 1603-1621.
- Brace, W.F., and Kohlstedt, D.L., 1980, Limits on lithospheric stress imposed by laboratory experiments: *Journal of Geophysical Research*, v. 85, no. B11, p. 6248-6252.
- Clark, J.C., Brabb, E.E., and McLaughlin, R.J., 1989, Geologic map and structure sections of the Laurel $7\frac{1}{2}'$ Quadrangle, Santa Clara and Santa Cruz counties, California: U.S. Geological Survey Open-File Report 89-676, 31 p., scale 1:24,000, 2 sheets.
- Dahlstrom, D.C.A., 1969, Balanced cross sections: *Canadian Journal of Earth Sciences*, v. 6, no. 4, pt. 1, p. 743-757.
- Dietz, L.D., and Ellsworth, W.L., 1990, The October 17, 1989, Loma Prieta, California, earthquake and its aftershocks; geometry of the sequence from high-resolution locations: *Geophysical Research Letters*, v. 17, no. 9, p. 1417-1420.
- Eberhart-Phillips, D.M., Labson, V.F., Stanley, W.D., Michael, A.J., and Rodriguez, B.D., 1990, Preliminary velocity and resistivity models of the Loma Prieta earthquake region: *Geophysical Research Letters*, v. 17, no. 8, p. 1235-1238.
- Erickson, L., 1987, User's manual for DIS3D, a three-dimensional displacement program with application to faulting in the earth: Stanford, Calif., Stanford University, Department of Applied Earth Sciences, 167 p.
- Johnson, A.M., 1977, *Styles of folding; mechanics and mechanisms of folding of natural elastic materials*: New York, Elsevier, 406 p.
- King, G.C.P., Stein, R.S., and Rundle, J.B., 1988, The growth of geological structures by repeated earthquakes, 1. Conceptual framework: *Journal of Geophysical Research*, v. 93, no. B11, p. 13307-13318.
- Lisowski, Michael, Prescott, W.H., Savage, J.C., and Johnson, M.J.S., 1990, Geodetic estimate of coseismic slip during the 1989 Loma Prieta, California, earthquake: *Geophysical Research Letters*, v. 17, no. 9, p. 1437-1440.
- Marshall, G.A., Stein, R.S., and Thatcher, Wayne, 1991, Faulting geometry and slip from co-seismic elevation changes: the 18 October 1989 Loma Prieta, California, earthquake: *Seismological Society of America Bulletin*, v. 81, no. 5, p. 1660-1693.
- McLaughlin, R.J., Clark, J.C. and Brabb, E.E., 1988, Geologic map and structure sections of the Loma Prieta $7\frac{1}{2}'$ quadrangle, Santa Clara and Santa Cruz counties, California: U.S. Geological Survey Open-

File Report 88-752, 32 p., scale 1:24,000, 2 sheets.

- Oppenheimer, D.H., 1990, Aftershock slip behavior of the 1989 Loma Prieta, California earthquake: *Geophysical Research Letters*, v. 17, no. 8, p. 1199-1202.
- Oppenheimer, D.H., Reasenber, P.A., and Simpson, R.W., 1988, Fault plane solutions for the 1984 Morgan Hill, California, earthquake sequence; evidence for the state of stress on the Calaveras Fault: *Journal of Geophysical Research*, v. 93, no. B8, p. 9007-9026.
- Plafker, George, and Galloway, J.P., eds., 1989, Lessons learned from the Loma Prieta, California, earthquake of October 17, 1989: U.S. Geological Survey Circular 1045, 48 p.
- Ponti, D.J., and Wells, R.E., 1991, Off-fault ground ruptures in the Santa Cruz Mountains, California; ridge-top spreading versus tectonic extension during the 1989 Loma Prieta earthquake: *Seismological Society of America Bulletin*, v. 81, no. 5, p. 1480-1510.
- Prucha, J.J., Graham, J.A., and Nickelsen, R.P., 1965, Basement-controlled deformation in Wyoming province of Rocky Mountains foreland: *American Association of Petroleum Geologists Bulletin*, v. 49, no. 7, p. 966-992.
- Reches, Ze'ev, 1978, Development of monoclines; part I. Structure of the Palisades Creek branch of the East Kaibab monocline, Grand Canyon, Arizona, in Matthews, Vincent, III, ed., *Laramide folding associated with basement block faulting in the western United States: Geological Society of America Memoir 151*, p. 235-271.
- Reches, Ze'ev, and Johnson, A.M., 1978, Development of monoclines; part II. Theoretical analysis of monoclines, in Matthews, Vincent, III, ed., *Laramide folding associated with basement block faulting in the western United States: Geological Society of America Memoir 151*, p. 273-311.
- Reches, Ze'ev, Hoexter, D.F. and Hirsch, Francis, 1981, The structure of a monocline in the Syrian Arc system, Middle East; surface and subsurface analysis: *Journal of Petroleum Geology*, v. 3, no. 3, p. 413-425.
- Sanford, A.R., 1959, Analytical and experimental study of simple geologic structures: *Geological Society of America Bulletin*, v. 70, no. 1, p. 19-52.
- Sarna-Wojcicki, A.M., Pampeyan, E.H., and Hall, N.T., 1975, Map showing recent active breaks along the San Andreas fault between central Santa Cruz Mountains and the northern Gabilan Range, California: U.S. Geological Survey Miscellaneous Field Studies Map MF-650, scale 1:24,000, 2 sheets.
- Stearns, D.W., 1978, Faulting and forced folding in the Rocky Mountains foreland, in Matthews, Vincent, III, ed., *Laramide folding associated with basement block faulting in the western United States: Geological Society of America Memoir 151*, p. 1-37.
- Stein, R.S., and King, G.C.P., 1984, Seismic potential revealed by surface folding; 1983 Coalinga, California, earthquake: *Science*, v. 224, no. 4651, p. 869-872.

$$\frac{\partial^4 \Psi}{\partial x^4} + 2 \frac{\partial^4 \Psi}{\partial x^2 \partial y^2} + \frac{\partial^4 \Psi}{\partial y^4} = 0. \quad (1)$$

The general solution for Ψ is

$$\Psi = \frac{1}{\lambda} \left\{ [a + b(\lambda y - 1)] \exp(\lambda y) - [c + d(\lambda y + 1)] \exp(-\lambda y) \right\} \cos(\lambda x), \quad (2a)$$

$$\text{where} \quad \lambda = 2\pi n/L, \quad (2b)$$

L is the longest wavelength, n is an integer indicating higher harmonic ($n=1 \dots N$), and a , b , c , and d are constants to be determined from the boundary conditions. The formulas for the stresses, displacements and strains in the layers are derived from equations 2 (Reches and Johnson, 1978, app. 1). To generate the step geometry of the basement faulting we superposed as many as 180 wavelengths, as described below (also see Reches and Johnson (1978, app. 2).

The normal and shear stresses written for the i th layer and the n th wavelength are given by

$$\sigma_{xx} = 2\mu\lambda \left\{ [a_i + b_i(\lambda y - 1)] \exp(\lambda y) + [c_i + d_i(\lambda y + 1)] \exp(-\lambda y) \right\} \sin(\lambda x) - \rho y \quad (3a)$$

$$\sigma_{yy} = -2\mu\lambda \left\{ [a_i + b_i(\lambda y + 1)] \exp(\lambda y) + [c_i + d_i(\lambda y - 1)] \exp(-\lambda y) \right\} \sin(\lambda x) - \rho y \quad (3b)$$

$$\sigma_{xy} = 2\mu\lambda \left\{ (a_i + b_i \lambda y) \exp(\lambda y) - (c_i + d_i \lambda y) \exp(-\lambda y) \right\} \cos(\lambda x); \quad (3c)$$

the horizontal displacement u and vertical displacement v by

$$u = [(a_i + b_i \lambda y) \exp(\lambda y) + (c_i + d_i \lambda y) \exp(-\lambda y)] \cos(\lambda x) \quad (4a)$$

$$v = \left\{ [(a_i + b_i(\lambda y - l))] \exp(\lambda y) - [c_i + d_i(\lambda y + l)] \exp(-\lambda y) \right\} \sin(\lambda x) \quad (4b)$$

APPENDIX: ANALYTICAL PROCEDURE

The mechanical deformation within a fault-fold system is derived here for the deformation of incompressible elastic or viscous layers overlying a faulted basement; the deformation is plane strain, restricted to the x - y plane (fig. 1). According to Reches and Johnson (1978, app. 1, eq. 10), the stress-strain relations, equilibrium equations, and compatibility equations are satisfied if the stress function Ψ satisfies the biharmonic equation

and the normal and shear strains by

$$\varepsilon_{xx} = -\lambda \left[(a_i + b_i \lambda y) \exp(\lambda y) + (c_i + d_i \lambda y) \exp(-\lambda y) \right] \sin(\lambda x) \quad (5a)$$

$$\varepsilon_{yy} = -\varepsilon_{xx} \quad (5b)$$

$$\varepsilon_{xy} = -\lambda \left[(a_i + b_i \lambda y) \exp(\lambda y) + (c_i + d_i \lambda y) \exp(-\lambda y) \right] \cos(\lambda x) \quad (5c)$$

where μ is the shear modulus, n is an integer indicating the wavelength ($n=1 \dots N$), L is the longest wavelength considered, and a_i , b_i , c_i , and d_i are constants of the i th layer that depend on the geometry, properties, and boundary conditions of the problem.

The above equations indicate that the stresses, displacements, and strains in the i th layer are completely specified by four constants a_i , b_i , c_i , and d_i . Thus, four boundary conditions are needed for each layer to solve for the deformation. The boundary conditions are specified at the contacts between layers and are based on the continuity of stresses and displacements. For bonded contacts, the conditions at the contacts are

$$\{\sigma_{yy}\}_i = \{\sigma_{yy}\}_{i-1}, \quad (6a)$$

$$\{\sigma_{xy}\}_i = \{\sigma_{xy}\}_{i-1}, \quad (6b)$$

$$u_i = u_{i-1} \quad (6c)$$

$$v_i = v_{i-1}, \quad (6d)$$

and for free-to-slip contacts, the conditions at the contacts are

$$\{\sigma_{yy}\}_i = \{\sigma_{yy}\}_{i-1} \quad (7a)$$

$$\{\sigma_{xy}\}_i = 0 \quad (7b)$$

$$\{\sigma_{xy}\}_{i-1} = 0 \quad (7b)$$

$$v_i = v_{i-1}. \quad (7d)$$

The boundary conditions at the top of the model that is a stress-free surface are

$$\{\sigma_{yy}\}_{\text{top}} = 0, \quad (8b)$$

$$\{\sigma_{xy}\}_{\text{top}} = 0. \quad (8b)$$

The boundary conditions at the base of the layered sequence are presented in the next section (eqs. 9).

It can be shown that these boundary conditions generate $4K$ linear equations where K is the number of layers. This system is solved simultaneously to obtain the constants a_i , b_i , c_i , and d_i for all layers. These constants are then substituted into the stress and displacement equations to calculate the required deformation parameter, as follows.

CALCULATION AND PRESENTATION PROCEDURES

A set of dedicated computer programs based on the above analytical solutions were written in QuickBasic for the IBM PC. The programs are interactive, and their results are graphically presented on the screen. The programs includes five main steps as follows.

In the first step, the sequence of layers is selected. The number of layers ranges from 1 to 10, the thickness of the layers is unrestricted, and the contacts between them may be either bonded or free to slip.

In the second step, the basal displacement, which is the displacement of the base of the layered sequence, is calculated. This displacement reflects the slip along the fault (reverse or normal and inclination) and the deformation of the basement. We solve here for two classes of basal displacements. In the first class, the basement is approximated by perfectly rigid blocks with no internal deformation, separated by a weak fault. This approximation is based on field observations that indicate the planar geometry of basement blocks (Reches and Johnson, 1978; see section above entitled "Analysis of a Fold-Fault System"). The vertical displacement V_x and the horizontal displacement U_x at the base of the layered sequence are determined by the following Fourier series for a step:

$$V_{x(\text{base})} = V_0 \sum_n \frac{4}{n\pi} \sin^2\left(\frac{n\pi}{4}\right) \sin\left(\frac{\pi n}{\lambda}\right) \quad (9a)$$

$$\text{and } U_{x(\text{base})} = U_0 \sum_n \frac{2}{n\pi} (-1)^n \sin^2\left(\frac{n\pi}{2}\right) \cos\left(\frac{\pi x}{\lambda}\right), \quad (9b)$$

where $\lambda = 2\pi n / L$, ($n = 1, 2, \dots, N$)

L is the longest wavelength considered (typically, 160 km in the present modeling), N is the maximum number of Fourier components considered ($N=100-200$), and V_0 and U_0 are the maximum vertical and horizontal displacements, respectively. $U_0=0$ indicates slip along a vertical fault, $U_0=V_0$ indicates slip along a 45°-dipping reverse fault, and $U_0=-V_0$ indicates slip along a 45°-dipping normal fault.

The second class of basal displacement, for a single earthquake, combines fault slip and the elastic deformation of the basement. To calculate this combined deformation, we used the computer program DIS3D (Erickson, 1987), which calculates the displacements, strains, and stresses in an elastic half-space due to slip along one or more dislocations. The selected fault slip and fault inclination were substituted into the program, and the displacements were calculated for plane-strain conditions. The basal displacements along a horizontal surface that is at the depth of the base of the layered sequence (generally, 5-km depth) are then transformed into a Fourier series in which the vertical component is the sine series and the horizontal component is the cosine series. We used 100 to 200 waves to obtain a good approximation of the displacement. The results of this transformation are substituted into the analytical solution of the layered sequence as the basal-displacement boundary condition. In so doing, we assume that the displacements at the top of the basement (that is, the base of the layers) due to slip along a fault embedded within it are only slightly affected by the layering above the basement.

The third step is the main computation stage. The stress and displacement equations (eqs. 3, 4) are substituted into the boundary conditions between the layers (eq. 6 or 7), at the top (eq. 8), and at the base (eq. 9). The 4K linear equations for each wavelength are solved simultaneously to determine the set of unknown constants a_i , b_i , c_i , and d_i . These process is repeated for all N wavelengths. Now, the stresses and displacement (eqs. 3, 4) can be calculated for every point within the layered sequence by summation of the N waves' contributions. The results are presented in cross sections that include the displacements and the orientation of the maximum-compressive-stress axes and the intensity of the shear stress (figs. 3, 6, 7).

The distribution and mode of aftershocks could serve as indicators for the slip during the earthquake and preearthquake stresses (Oppenheimer and others, 1988). The aftershocks of the Loma Prieta earthquake display a rather-confusing distribution of focal-plane solutions, with focal solutions of reverse faulting side by side with normal faulting or strike-slip events (Michael, 1991). Because this disorganized pattern persists also in the upper 5 km, we disregard here the focal solutions of the aftershocks and use their spatial distribution. This distribution is correlated with the intensity of the calculated shear stresses (see subsection above entitled "Aftershock Distribution").

The intensity of the shear stress is evaluated by the procedure of Brace and Kohlstedt (1980), who assumed that upper-crustal rocks yield by frictional slip according to Coulomb criteria, with the coefficients of Byerlee's law. Their equation 3 indicates that at a depth of a few kilometers, yielding occurs when

$$\tau = \frac{\sigma_1 - \sigma_3}{2} \approx 2\sigma_3, \quad (10)$$

where σ_1 and σ_3 are the magnitudes of the maximum and minimum compressive stresses (assuming that $\mu=0.85$). Because the lithostatic load strongly affects frictional sliding τ is divided by the lithostatic pressure to obtain the normalized shear stress,

$$\tau_E = -\frac{\sigma_1 - \sigma_3}{2\rho g Y}, \quad (11)$$

where ρ is the mean rock density, g is the acceleration due to gravity, and Y is the local depth. τ_E can be related to field conditions if the principal stresses are assumed to be horizontal and (or) vertical, in which case it can be shown that

$$\sigma_1 = \sigma_H > \sigma_h > \sigma_v = \sigma_3 \text{ for thrusting,}$$

$$\sigma_1 = \sigma_H > \sigma_v > \sigma_h = \sigma_3 \text{ for strike-slip conditions,}$$

$$\text{and } \sigma_1 = \sigma_v > \sigma_H > \sigma_h = \sigma_3 \text{ for normal faulting,}$$

where σ_H and σ_h are the maximum and minimum horizontal stresses and $\sigma_v = \rho g Y$ is the vertical stress. Substituting equation 10 and the conditions of the last three equations into equation 11 reveals that $\tau_E \geq 2$ for thrusting, $\tau_E \geq 1$ for strike-slip conditions, and $\tau_E \geq 0.4$ for normal faulting.

The above equations are for the total stresses, which include the unknown preearthquake stress; this stress is modified because of the slip during the earthquake. Oppenheimer and others (1988) selected various preearthquake stresses to calculate their failure parameter F (which is equivalent to the present parameter τ_E). Because the preearthquake stresses for the Loma Prieta region are unknown, we consider here only changes in the shear stresses. We anticipate that an increase in the shear stress would increase the tendency for local aftershocks. From equation 11, the change in the shear stress during the earthquake is defined as

$$\Delta\tau_E = -\frac{\Delta(\sigma_1 - \sigma_3)}{2\rho g Y}, \quad (12)$$

which is equivalent to the parameter ΔF of Oppenheimer and others (1988).

In the calculations presented here, we consider shear-stress changes to be significant if $\Delta\tau_E \geq 0.05\tau_E$ (see Oppenheimer and others, 1988, p. 9020-9021). Rock density is assumed to be uniformly equal to 2,650 kg/m³.